Structure
Article

Human IL-34 and CSF-1 Establish Structurally Similar Extracellular Assemblies with Their Common Hematopoietic Receptor

Jan Felix,[1,5] Jonathan Elegheert,[1,6] Irina Gutsche,[3] Alexander V. Shkumatov,[4] Yurong Wen,[2] Nathalie Bracke,[1,7] Erwin Pannecoucke,[1] Isabel Vandenberghe,[2] Bart Devreese,[2] Dmitri I. Svergun,[4] Ewald Pauwels,[5] Bjorn Vergauwen,[1] and Savvas N. Savvides[1,*]

[1]Unit for Structural Biology
[2]Unit for Biological Mass Spectrometry and Proteomics
Laboratory for Protein Biochemistry and Biomolecular Engineering (L-ProBE), Ghent University, K.L. Ledeganckstraat 35, 9000 Ghent, Belgium
[3]Unit of Virus Host Cell Interactions, UVHCI, UMI 3265 UJF-EMBL-CNRS, 6 rue Jules Horowitz, BP 181, 38042 Grenoble cedex 9, France
[4]Biological Small Angle Scattering Group, EMBL, Notkestraße 85, 22603 Hamburg, Germany
[5]Center for Molecular Modeling, Ghent University, Technologiepark 903, 9052 Zwijnaarde, Belgium
[6]Present address: Division of Structural Biology, Wellcome Trust Centre for Human Genetics, University of Oxford, Oxford OX3 7BN, UK
[7]Present address: Laboratory of Drug Quality and Registration, Department of Pharmaceutical Analysis, Ghent University, 9000 Ghent, Belgium
*Correspondence: savvas.savvides@ugent.be
http://dx.doi.org/10.1016/j.str.2013.01.018

SUMMARY

The discovery that hematopoietic human colony stimulating factor-1 receptor (CSF-1R) can be activated by two distinct cognate cytokines, colony stimulating factor-1 (CSF-1) and interleukin-34 (IL-34), created puzzling scenarios for the two possible signaling complexes. We here employ a hybrid structural approach based on small-angle X-ray scattering (SAXS) and negative-stain EM to reveal that bivalent binding of human IL-34 to CSF-1R leads to an extracellular assembly hallmarked by striking similarities to the CSF-1:CSF-1R complex, including homotypic receptor-receptor interactions. Thus, IL-34 and CSF-1 have evolved to exploit the geometric requirements of CSF-1R activation. Our models include N-linked oligomannose glycans derived from a systematic approach resulting in the accurate fitting of glycosylated models to the SAXS data. We further show that the C-terminal region of IL-34 is heavily glycosylated and that it can be proteolytically cleaved from the IL-34:hCSF-1R complex, providing insights into its role in the functional nonredundancy of IL-34 and CSF-1.

INTRODUCTION

The hematopoietic colony stimulating factor-1 receptor (CSF-1R or c-fms), a class III receptor tyrosine kinase (RTK-III) featuring five Ig-like extracellular domains (Lemmon and Schlessinger, 2010; Verstraete and Savvides, 2012), is activated by its two cytokine ligands, CSF-1 and interleukin 34 (IL-34), to establish signaling cascades leading to the proliferation, differentiation, and functionality of cells derived from the mononuclear phagocytic lineage, such as monocytes, tissue macrophages, microglia, osteoclasts, and antigen-presenting dendritic cells (Chitu and Stanley, 2006; Hamilton and Achuthan, 2012; Verstraete and Savvides, 2012). Furthermore, signaling via wild-type hCSF-1R and mutants thereof has been implicated in a wide range of pathologies in humans, such as arthritis, atherosclerosis, tumor growth, and metastasis (Verstraete and Savvides, 2012).

Over the last decade the molecular basis of CSF-1R activation has taken an unexpected twist when *csf1r* $^{-/-}$ mice were found to exhibit a stronger phenotype than *csf1*$^{op/op}$ mice (Dai et al., 2002), which suggested the possibility of CSF-1-independent activation of CSF-1R. Thus, the recent discovery that IL-34, a cytokine sharing no recognizable sequence similarity to the prototypical CSF-1R ligand CSF-1 (Lin et al., 2008), serves as a second ligand to CSF-1R essentially established CSF-1R as perhaps the most intriguing member of the RTK-III family. IL-34 can fully rescue the phenotype of *csf1*$^{op/op}$ mice when expressed in a CSF-1-specific manner (Wei et al., 2010), and like CSF-1, IL-34 stimulates monocyte survival, macrophage proliferation, osteoclast formation/differentiation, and is involved in the development of microglia (Baud'huin et al., 2010; Lin et al., 2008; Mizuno et al., 2011). Despite such seemingly functional equivalence, important differences do exist. For instance, IL-34 causes a stronger and more rapidly declining phosphorylation of CSF-1R when compared to CSF-1 (Chihara et al., 2010). Moreover, analysis of mRNA expression levels in embryonic and adult mouse tissues revealed that IL-34 is expressed differentially from CSF-1, resulting in higher IL-34 mRNA levels in the postnatal and adult brain, salivary glands, and ear (Wei et al., 2010). Finally, recent studies have identified additional functionalities for IL-34 as a key growth factor for the development of Langerhans cells from myeloid cells in the skin (Greter et al., 2012; Wang et al., 2012).

The duality of CSF-1R activation and the lack of sequence homology between CSF-1 and IL-34, inevitably established

a structural conjecture as to possible differences and similarities in the structural basis of CSF-1R activation by IL-34 and CSF-1. Structural studies on human and mouse CSF-1R ectodomains in complex with cognate CSF-1 demonstrated that despite the restrictive species cross-reactivity of CSF-1 and CSF-1R (Garceau et al., 2010; Gow et al., 2012a, 2012b), CSF-1:CSF-1R complexes share important commonalities (Chen et al., 2008; Elegheert et al., 2011). These are hallmarked by the bivalent binding of CSF-1 to CSF-1R to establish interaction interfaces with extracellular Ig-like domains D2 and D3 in CSF-1R and the ensuing homotypic receptor-receptor interaction between the membrane-proximal D4 domains of CSF-1R. In addition, the elucidation of the mechanism by which the viral decoy receptor BARF1 allosterically inactivates human CSF-1 has led to a deconvolution of the cooperative and modular character of CSF-1:CSF-1R complexes (Elegheert et al., 2012).

We here build on recent exciting developments in the structural biology of human and mouse IL-34:CSF-1R complexes that revealed the structure of the IL-34 core (a construct devoid of 50 C-terminal residues) and the structural details of its interaction with the first three extracellular domains of CSF-1R (CSF-1R$_{D1-D3}$) (Liu et al., 2012; Ma et al., 2012). In particular, our study has sought to provide structural insights into the assembly principles underlying the complete human IL-34:CSF-1R extracellular complex and to investigate the possibility of a structural consensus between IL-34 and CSF-1 complexes with their common receptor. Such insights would complete an unprecedented series of snapshots of full-length RTK-III ectodomains in complex with their cognate helical cytokines (Elegheert et al., 2011; Verstraete et al., 2011b; Yuzawa et al., 2007), thereby establishing the repertoire of their structural and mechanistic features (Verstraete and Savvides, 2012). This has become especially important at a time when somatic mutations identified in RTK-III ectodomains continue to emerge from genomic analyses of tumor and cancer cells (Verstraete and Savvides, 2012). In parallel, our study addresses the role and structural characteristics of the C-terminal tail of IL-34, a 50-residue sequence that has been excluded from all previous structural studies.

RESULTS

Isolation and Biochemical Characterization of IL-34 Complexes with CSF-1R Ectodomains

Production of recombinant human hIL-34 and hCSF-1R ectodomain variants (Elegheert et al., 2011) for structural studies was initially carried out via transient expression in HEK293T cells in the presence of kifunensine (Chang et al., 2007). However, yields for the two target constructs of IL-34, i.e., full-length hIL-34 (hIL-34$_{FL}$) and hIL-34$_{N21-P200}$ featuring a C-terminal deletion to exclude the predicted inherently unstructured region (Yang et al., 2005), were prohibitively low. To circumvent this problem, we established stable tetracycline-inducible HEK293S GnTI$^{-/-}$ cell lines (Reeves et al., 2002; Verstraete et al., 2011a) expressing high amounts of recombinant hIL-34 (typically 2 mg per liter of expression medium), which offered the additional benefit of homogeneous N-linked glycosylation with $GlcNAc_2Man_5$. We further exploited this key tool to produce IL34:CSF-1R complexes (hIL34:hCSF-1R$_{D1-D3}$ and hIL34:hCSF-1R$_{D1-D5}$) by transfecting our stable cell lines expressing IL-34 with the appropriate receptor construct. The ensuing purification of recombinant hIL-34:hCSF-1R complexes by immobilized metal affinity chromatography (IMAC) and size-exclusion chromatography (SEC) led to highly monodisperse preparations approaching yields of 1 mg per liter of expression medium (Figure 1A).

To probe the possible stoichiometry of our recombinant complexes, multiangle laser light scattering (MALLS) experiments were carried out using a force field fractionation (FFF) module (Figure 1B). Our analysis revealed molecular weights that are consistent with predicted N- and O-linked glycosylation in IL-34 and CSF-1R (Gupta et al., 2004; Julenius et al., 2005) and strongly suggested that all three recombinant complexes correspond to ternary assemblies whereby dimeric hIL-34 ligand binds two receptor molecules.

Structure of the Complete Extracellular Assembly of the IL-34:CSF-1R Complex

To elucidate the extracellular assembly of the hIL-34:hCSF-1R$_{D1-D5}$ complex, we pursued a combined approach featuring structural characterization of hIL-34:hCSF-1R complexes in solution via SAXS and direct visualization of the complex using negative stain electron microscopy (EM).

We used highly monodisperse preparations of purified recombinant hIL-34$_{FL}$:hCSF-1R$_{D1-D5}$ and hIL-34$_{N21-P200}$:hCSF-1R$_{D1-D5}$ to measure SAXS data at several concentrations of the complex (Figures S1A and S1B available online). Despite the overall good quality of both SAXS data sets (Table S1; Figures S1A and S1B), we were only able to obtain robust ab initio models with good clustering behavior for the hIL-34$_{N21-P200}$:hCSF-1R$_{D1-D5}$ complex. The predicted inherent structural flexibility and heavy glycosylation of the long C-terminal tail are likely reasons for this behavior. Nonetheless, we note that the distance distribution functions for hIL-34$_{FL}$:hCSF-1R$_{D1-D5}$ and hIL-34$_{N21-P200}$:hCSF-1R$_{D1-D5}$ complexes suggest adoption of similar shapes by the two complexes (Figure S1E), albeit with the hIL-34$_{FL}$:hCSF-1R$_{D1-D5}$ complex being slightly larger as indicated by the D_{max} and I_0 values (Figures S1E and S1F). This suggests that the C-terminal 50 residues in hIL-34 do not substantially contribute to the overall shape of the complex and that they likely adopt a highly flexible structure. Ab initio modeling of the hIL-34$_{N21-P200}$:hCSF-1R$_{D1-D5}$ complex led to a molecular envelope featuring a central triangular toroid decorated with appendages at each vertex (Figure S2A). We subsequently used available crystal structures for hIL-34$_{N21-V193}$ and complexes thereof with hCSF-1R$_{D1-D3}$ (Ma et al., 2012) and homology models for hCSF-1R$_{D4}$ and hCSF-1R$_{D5}$ derived from KIT (Yuzawa et al., 2007) to reconstruct the assembly of the hIL-34$_{N21-P200}$:hCSF-1R$_{D1-D5}$ complex (Figure 2) by restrained rigid-body modeling. A key methodological implementation in our modeling approach concerned the inclusion of N-linked oligomannose glycans ($GlcNAc_2Man_5$) and missing loop regions (Choi and Deane, 2010), which were optimized with the help of molecular dynamics and energy-minimization protocols (Phillips et al., 2005). We based our selection of candidate N-linked glycosylation sites on the crystal structure of hIL-34$_{N21-V193}$:hCSF-1R$_{D1-D3}$, which clearly shows electron density for the first GlcNAc residue at residues Asn75 in hIL34$_{N21-V193}$ and Asn73, Asn153, Asn240, and Asn275 in hCSF-1R$_{D1-D3}$. In particular,

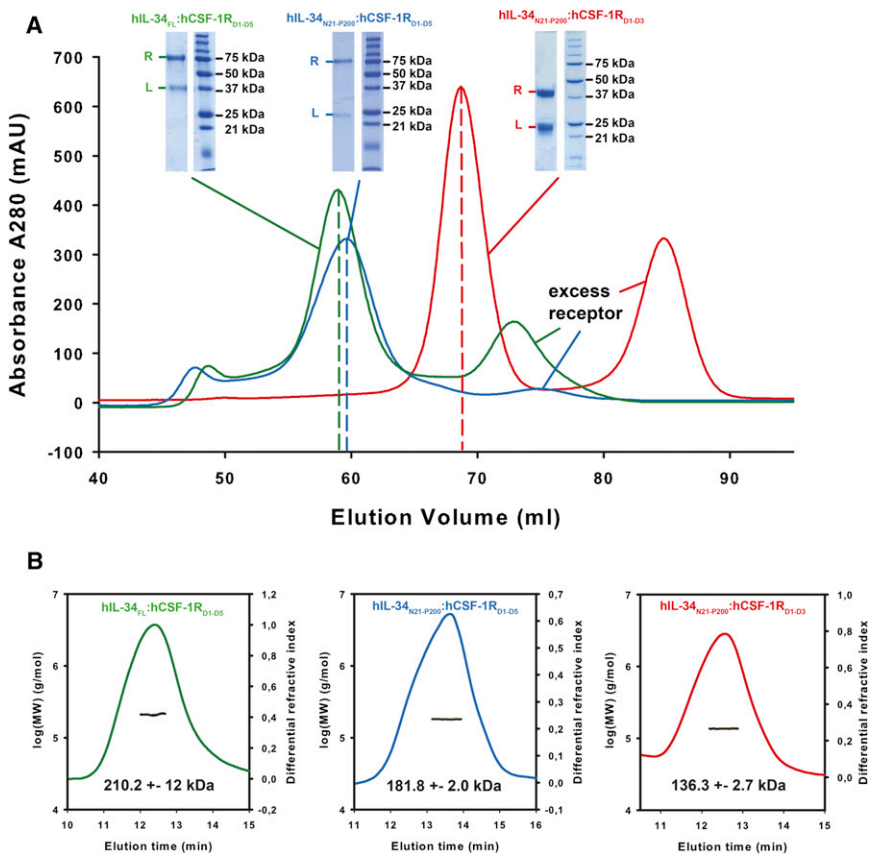

Figure 1. Biochemical Characterization of hIL-34$_{FL}$:hCSF-1R$_{D1-D5}$, hIL-34$_{N21-P200}$:hCSF1-R$_{D1-D5}$, and hIL-34$_{N21-P200}$:hCSF-1R$_{D1-D3}$ Complexes

(A) SEC profiles of hIL-34$_{FL}$:hCSF-1R$_{D1-D5}$ (green), hIL-34$_{N21-P200}$:hCSF-1R$_{D1-D5}$ (blue), and hIL-34$_{N21-P200}$:hCSF-1R$_{D1-D3}$ (red) complexes. The profiles are accompanied by insets showing SDS-PAGE analysis of peak fractions (R, receptor; L, ligand). Details on purification of the complexes can be found in the Experimental Procedures.

(B) Molecular weight determination of hIL-34$_{FL}$:hCSF-1R$_{D1-D5}$ (green), hIL-34$_{N21-P200}$:hCSF-1R$_{D1-D5}$ (blue), and hIL-34$_{N21-P200}$:hCSF-1R$_{D1-D3}$ (red) by MALLS. The differential refractive index signal of the different complexes is plotted as a function of the elution time after FFF. The derived molecular weights are shown together with the fits (black lines) to the MALLS data.

we note that modeling of glycan trees, accounting for almost 10% of the total scattering mass (Table S1), provided dramatic improvements in the agreement between models and experimental data (Figure 2A; Table S1) and has essentially been a crucial experimental parameter.

The structure of the hIL-34$_{N21-P200}$:hCSF-1R$_{D1-D5}$ complex as derived from SAXS data revealed a ternary assembly in which an IL-34 dimer bivalently binds to two copies of CSF-1R evoking homotypic D4-D4' receptor contacts Figures 2A and 2B). CSF-1R employs D2 and D3 to form the cytokine binding site. At the same time, the N-terminal D1 domains of CSF-1R emanate outward without making any contacts with other components of the complex, whereas the membrane-proximal D5 domains diverge from each other without contacting one another (Figure 2B). We further note that the glycan trees also largely diverge away from the body of the complex, suggesting that they are not involved in specific interactions with components of the complex.

Parallel to structural studies of the complex by SAXS, we sought to image full-length human IL-34 (hIL-34$_{FL}$) in complex with hCSF-1R$_{D1-D5}$ via negative stain EM. The added value of this undertaking was the possibility to structurally probe for the first time the complex of intact hIL-34 with the complete ectodomain of hCSF-1R and to cross-validate the structural features revealed by our SAXS analysis of truncated IL-34 in complex with hCSF-1R. Imaging of negative-stained hIL-3 4$_{FL}$:hCSF-1R$_{D1-D5}$ (Figure 1), followed by multivariate statistical analysis (MSA) and classification of about 12,000 particles, resulted in a set of class averages featuring pronounced similarities to our models of the hIL-34$_{N21-P200}$:hCSF-1R$_{D1-D5}$ complex as derived from SAXS data (Figure 2C). To better compare these class averages with the models derived from SAXS, the classes were oriented to matching projections of the hIL-34$_{N21-P200}$:hCSF-1R$_{D1-D5}$ model filtered to 30 Å resolution. Our analysis reveals that all major features observed in the SAXS models are well conserved in the EM class averages (Figure 2C). Furthermore, the EM classes are devoid of additional features that could correspond to the C-terminal tail of hIL-34, lending further support to the flexibility of this region.

Encouraged by our approach for obtaining accurate SAXS-derived glycosylated models of cytokine-receptor complexes, we wondered whether it would be possible to obtain a complete model for the hCSF-1:hCSF-1R$_{D1-D5}$ complex from analysis of SAXS data. The architecture of this complex was recently characterized by three-dimensional (3D)-reconstruction of negatively stained images of the complex obtained by EM (Elegheert et al., 2011). Indeed, addition of N-linked glycans, in conjunction with a careful restraints model taking into account known interaction interfaces in the hCSF1:hCSF-1R complex, led to a model that agreed very well with experimental data (Figure 3A). Superposition of this model to the EM density map for the hCSF-1:hCSF-1R$_{D1-D5}$ complex (Elegheert et al., 2011) shows that the overall features and architecture of the complex are largely similar (Figure 3B), thus lending support to such dual approach for characterizing macromolecular assemblies.

To verify whether the proposed models for hIL-34:CSF-1R$_{D1-D5}$ and hCSF-1:CSF1R$_{D1-D5}$ would be consistent throughout different modeling runs against the experimental SAXS data, ten identical SASREF refinement protocols each with a distinct seed number were carried out in parallel for the two assemblies (Figure S3). Our results show that the core of the complexes defined by the bound cytokines and hCSF-1R$_{D2-D4}$, refined to nearly identical structures in all models, with glycans on CSF-1R$_{D2-D4}$ pointing consistently outward. Interestingly, D1

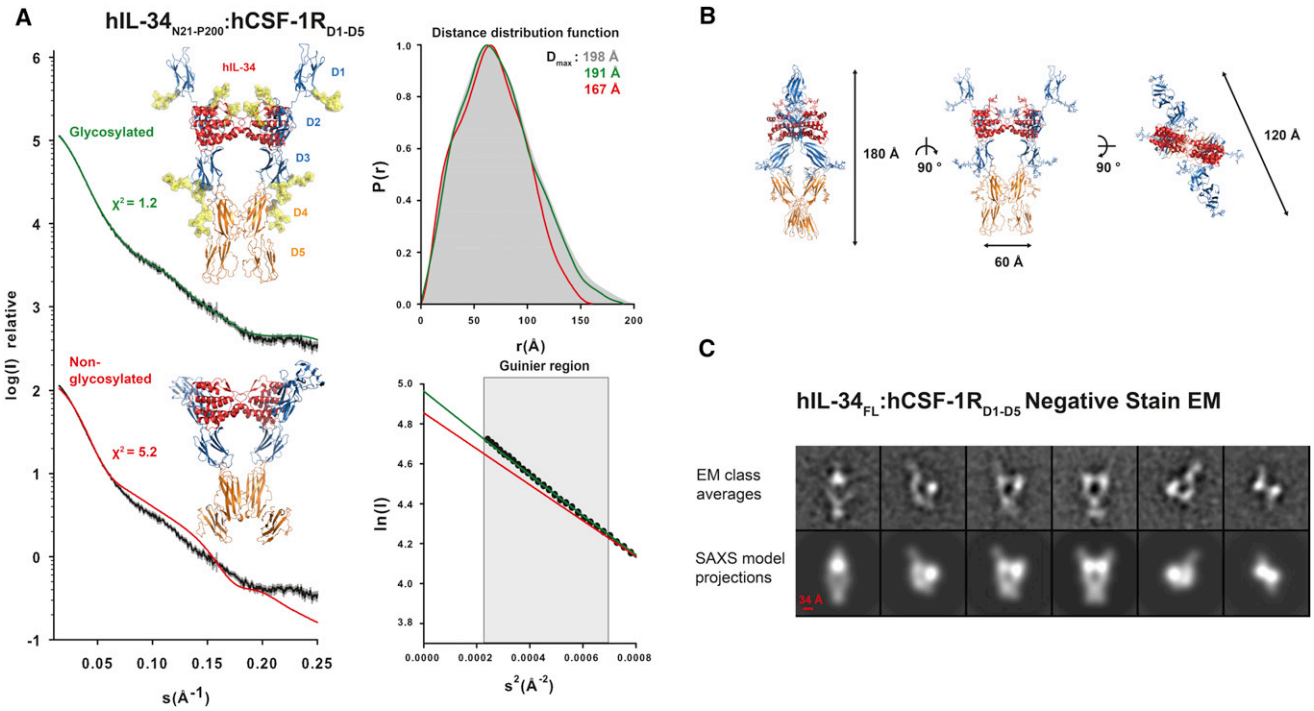

Figure 2. Structural Analysis of the hIL-34:hCSF-1R$_{D1-D5}$ Complex by SAXS and Negative Stain EM

(A) SAXS analysis of hIL-34$_{N21-P200}$:hCSF-1R$_{D1-D5}$. The left panel shows calculated scattering curves for hIL-34$_{N21-P200}$:hCSF-1R$_{D1-D5}$ rigid-body models generated by SASREF and their fits to the experimental data (black curves). The different fits are put on a relative scale for better visualization. The red curve represents the calculated curve from a SASREF-generated rigid-body model for hIL-34$_{N21-P200}$:hCSF-1R$_{D1-D5}$ using hIL-34$_{N21-V193}$:hCSF-1R$_{D2-D3}$ (PDB ID code 4DKD) as a rigid core, while allowing hCSF-1R$_{D1}$ to move by using distance restraints between hCSF1-R$_{D1}$ and hCSF-1R$_{D2}$. hCSF-1R$_{D4}$ and hCSF-1R$_{D5}$ were modeled by I-Tasser using D4 and D5 of the KIT receptor (PDB ID code 2E9W) as templates. Additional distance restraints were specified between hCSF-1R$_{D3}$ and hCSF-1$_{D4}$, between hCSF-1R$_{D4}$ and hCSF-1$_{D5}$, and between neighboring hCSF-1R$_{D4}$ domains. The green curve represents the calculated curve from a SASREF-generated rigid-body model using the same restraints as described above but with added GlcNAc$_2$Man$_5$ N-glycans on N75 of hIL34$_{N21-V193}$ and N73, N153, N240, N275, and N353 of hCSF-1R$_{D1-D5}$ (yellow). The upper-right panel shows the calculated distance distribution of the different hIL-34$_{N21-P200}$:hCSF-1R$_{D1-D5}$ SASREF models (red, without N-glycans; green, with N-glycans) and the distance distribution function of the experimental data in gray. Distance distribution functions were scaled to unity allowing better comparison. The lower-right panel shows calculated Guinier regions of the different hIL-34$_{N21-P200}$:hCSF-1R$_{D1-D5}$ SASREF models (red, without N-glycans; green, with N-glycans) and the Guinier region of the experimental data in black. The data range used for fitting is indicated as a light-gray box. See also the Experimental Procedures; Table S1; Figure S1.

(B) Three representative views of the hIL-34$_{N21-P200}$:hCSF-1R$_{D1-D5}$ complex in ribbon representation as derived from SAXS data.

(C) Negative stain EM of the hIL-34$_{FL}$:hCSF-1R$_{D1-D5}$ complex. Representative EM class averages (upper row) are shown along with projections of the rigid-body SAXS model for hIL-34$_{N21-P200}$:hCSF-1R$_{D1-D5}$ (lower row) blurred to 30 Å resolution for visual comparison. See also Figures S2 and S3; Table S3.

and D5 of CSF-1R adopted markedly more variable conformational states about the D1-D2 and D4-D5 hinge regions, resulting in an ensemble of structures (Figure S3). We note that in each case D1-D1′ and D5-D5′ pairs concertedly point away from the central axis of the complex at various degrees of separation without making any contacts in any case. Nonetheless, each of the models in the clusters fitted equally well to the data (IL-34:CSF-1R, mean χ^2 = 0.97 ± 0.13; CSF-1:CSF-1R, mean χ^2 = 1.11 ± 0.17) and showed a highly similar overall shape (Figure S3), corroborating the robustness of our individual models.

Although our study highlights the importance of including glycans in the SAXS modeling of glycosylated proteins, surprisingly only a handful of studies have adopted similar approaches. For instance, N-linked glycans can be added to the protein using the GlyProt server (Kajander et al., 2011; Rathore et al., 2012), they can be modeled as flexible residues using MODELER (Guttman et al., 2012), or they can be added as movable rigid bodies in SASREF (Alt et al., 2012; Zeev-Ben-Mordehai et al., 2009), although this approach is limited by the number of allowable rigid bodies. Our method allows effective modeling of glycans in glycosylated proteins against SAXS data by combining SASREF-based rigid-body modeling of starting structures, adding missing gaps/loops, and performing subsequent energy minimization runs to obtain stereochemically sound models. This modeling strategy can serve as an alternative option to the recently developed AllosMod-FoXS server, which combines MODELER-based glycan modeling with molecular dynamics optimization of generated ensembles using AllosMod (Weinkam et al., 2012), followed by comparisons of calculated scattering patterns to the experimental data using FoXS (Schneidman-Duhovny et al., 2010).

IL-34 Establishes a Ternary Complex in the Absence of the Receptor Membrane-Proximal Domains

In light of the recent crystal structure of hIL-34 in complex with hCSF-1R$_{D1-D3}$, describing a binary complex instead of the

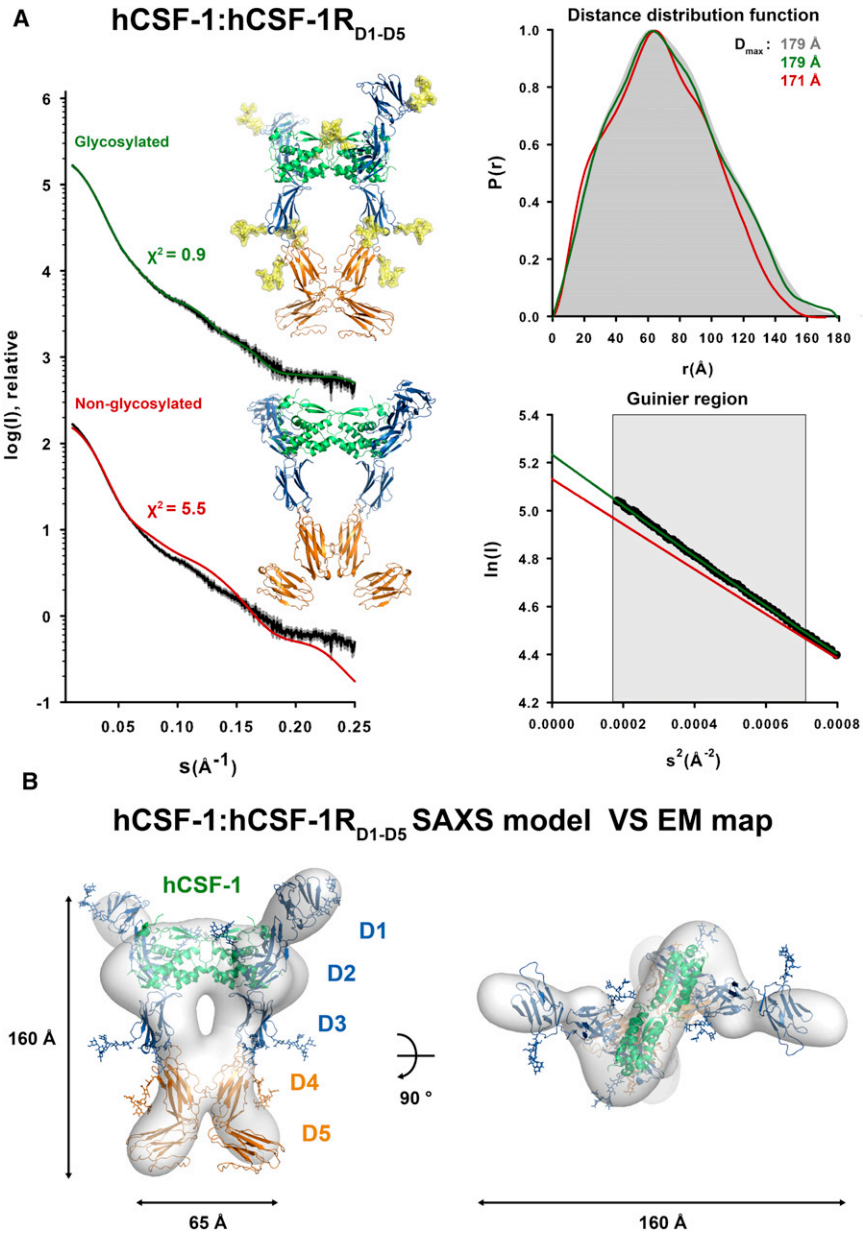

Figure 3. Structural Assembly of the hCSF-1:hCSF-1R$_{D1-D5}$ Complex Derived from SAXS Data

(A) A reanalysis of available SAXS data for the hCSF-1:hCSF-1R$_{D1-D5}$ complex. The left panel shows the fits between the experimental data (black curves) and calculated scattering curves for hCSF-1:hCSF-1R$_{D1-D5}$ rigid-body models generated by SASREF with (green) or without (red) modeled N-glycans, whereas the right panels show the distance distribution functions (upper-right) and Guinier region analysis (lower-right). Modeling was performed with identical restraints as described for hIL-34$_{N21-P200}$:hCSF-1R$_{D1-D5}$, except for the replacement of the hIL-34$_{N21-V193}$:hCSF-1R$_{D2-D3}$ rigid core by mouse CSF-1:CSF-1R$_{D2-D3}$ (Chen et al., 2008) (PDB ID code 3EJJ). See also the Experimental procedures; Table S1; Figure S1.

(B) Superposition of the rigid-body SAXS model and an EM density map for CSF-1:CSF-1R$_{D1-D5}$ (Elegheert et al., 2011) (the Electron Microscopy Data Bank accession code EMD-1977). The rigid-body SAXS model was manually placed in the EM density map (white). See also Figure S3; Table S3.

expected ternary assembly as suggested by binding studies via isothermal titration calorimetry (Ma et al., 2012) and a ternary complex for mouse IL-34:CSF-1R$_{D1-D3}$ (Liu et al., 2012), we pursued characterization of hIL-34$_{N21-P200}$:hCSF-1R$_{D1-D3}$ by SAXS. Indeed, fitting of the binary hIL-34$_{N21-V193}$:hCSF-1R$_{D1-D3}$ complex to the SAXS data revealed a gross incompatibility with the experimental scattering data (Figure 4, red curve). A systematic exploration of binary and ternary complexes derived from the crystal structure of hIL-34:hCSF-1R$_{D1-D3}$ and refined models thereof via restrained rigid-body refinement (including modeling of glycans and/or allowing flexibility of CSF-1R$_{D1}$) (Figure 4) showed that by far the best model was the glycosylated ternary assembly with hCSF-1$_{D1}$ pointing upward (Figure 4, green curve). This finding confirms that a stable ternary complex hIL-34:hCSF-1R$_{D1-D3}$ exists in solution, consistent with our MALLS analyses of the complex (Figure 1). We further note that the molecular architecture of this subcomplex is very similar to its counterpart in our full-length ectodomain complex (Figure 2).

The C-Terminal Region of IL-34 Is Heavily Glycosylated

Recent studies had shown that the last 40 residues at the C terminus of IL-34 are dispensable for receptor binding and activation (Chihara et al., 2010; Ma et al., 2012), yet no other biochemical or structural information has become available for this region. In fact, all available crystal structures for IL-34, either alone or in complex with CSF-1R$_{D1-D3}$, are based on truncated IL-34 constructs lacking this region. Indeed, a bioinformatics analysis to identify potential inherently disordered regions in full-length human and mouse IL-34 sequences (Yang et al., 2005) identifies a contiguous stretch of about 50 amino acids at the C terminus as a candidate inherently unstructured region, and subsequent prediction of N- and O-linked glycosylation indicates eight potential O-linked glycosylation sites (Julenius et al., 2005; Nishikawa et al., 2010) and no N-linked glycan sites.

We thus wondered what the domain character of this C-terminal segment might be and whether this segment might be glycosylated, according to predictions. Limited proteolysis experiments on the purified hIL-34$_{FL}$:hCSF-1R$_{D1-D5}$ complex (Figure 1) followed by staining of SDS-PAGE gels with Coomassie blue and glycostain led to a set of distinct molecular species (Figure 5A). On one hand, hIL-34 migrated as

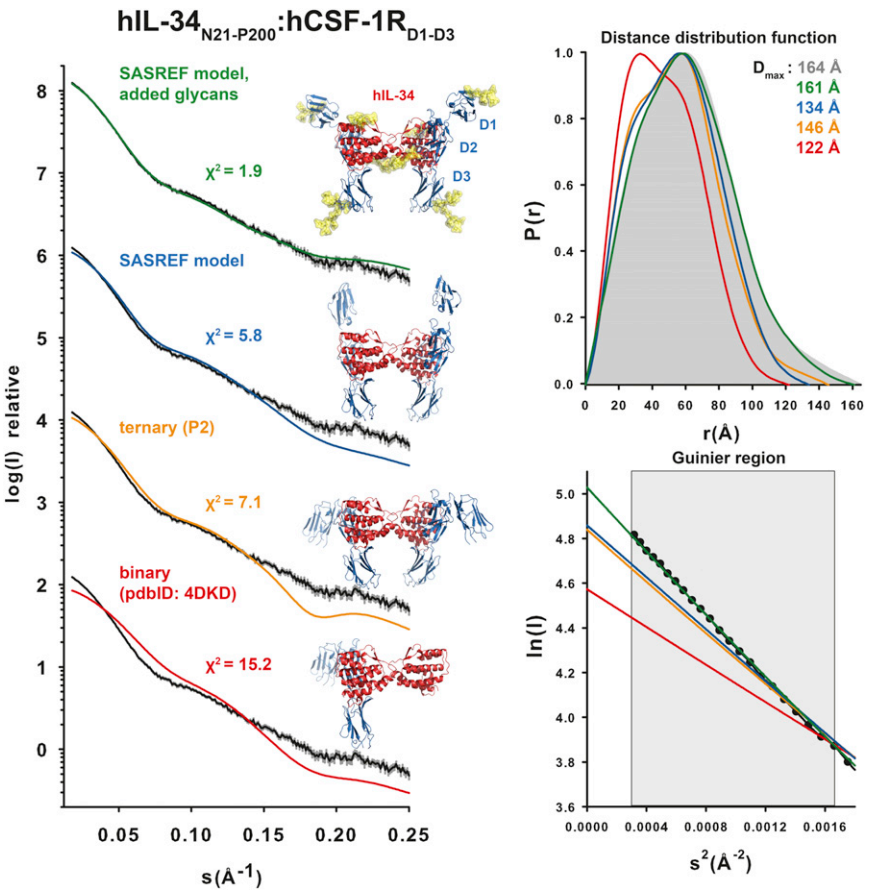

Figure 4. Structural Characterization the hIL-34$_{N21-P200}$:hCSF-1R$_{D1-D3}$ Ternary Complex

SAXS analysis of hIL-34$_{N21-P200}$:hCSF-1R$_{D1-D3}$. The left panel shows the fits between the experimental data (black curves) and calculated scattering curves for different hIL-34:hCSF-1R$_{D1-D3}$ structures/models along with their respective χ^2 values. The different fits are put on a relative scale for better visualization. The red curve shows the calculated curve from the crystal structure of the binary hIL-34$_{N21-V193}$:hCSF-1R$_{D1-D3}$ complex (Ma et al., 2012) (PDB ID code 4DKD). The orange curve shows the calculated curve from a generated ternary complex based on the hIL-34$_{N21-V193}$:hCSF-1R$_{D1-D3}$ crystal structure with a second hCSF-1R$_{D1-D3}$ molecule by applying 2-fold symmetry. The blue curve shows the calculated curve from a SASREF-generated rigid-body model using hIL-34$_{N21-V193}$:hCSF-1R$_{D2-D3}$ (PDB ID code 4DKD) as a rigid core, while allowing hCSF-1R$_{D1}$ to move by using 5 Å distance restraints between hCSF1-R$_{D1}$ and hCSF-1R$_{D2}$. The green curve shows the calculated curve from a SASREF-generated rigid-body model with identical restraints as the previous model (blue) but with added GlcNAc$_2$Man$_5$ N-glycans (shown in yellow) on N75 of hIL3434$_{N21-V193}$ and N73, N153, N240, and N275 of hCSF-1R$_{D1-D3}$. The upper-right panel shows the calculated distance distribution of the different hIL-34:hCSF-1R$_{D1-D3}$ structures/models (red, orange, blue, and green) and the distance distribution function of the experimental data in gray. Distance distribution functions were scaled to unity allowing better comparison. The lower-right panel shows calculated Guinier regions of the different hIL-34:hCSF-1R$_{D1-D3}$ structures/models (red, orange, blue, and green) and the Guinier region of the experimental data in black. The data range used for fitting is indicated as a light-gray box. See also the Experimental Procedures; Tables S1 and S3; Figures S1 and S2.

a ~25 kDa protein (hIL-34$_{TRUNC}$) compared to its native 35–40 kDa form, whereas hCSF-1R$_{D1-D5}$ was reduced to a ~50 kDa species (hCSF-1R$_{TRUNC}$) from its original apparent molecular weight of 75 kDa (Figure 5A). hIL-34$_{TRUNC}$ generated by limited proteolysis has the same electrophoretic mobility as our hIL-34$_{N21-P200}$ construct, which lacks the last 42 C-terminal residues. Despite the clear signal for hIL-34$_{FL}$ via Coomassie staining and glycan staining, and the preservation of good signal for hIL-34$_{TRUNC}$ via Coomassie staining, almost no signal is retained for hIL-34$_{TRUNC}$ according to glycan staining. This indicates that truncation of hIL-34$_{FL}$ to hIL-34$_{TRUNC}$ results in a drastic reduction of glycan content. To identify the domain composition of these truncated IL-34 and CSF-1R species, a mass spectrometric analysis was performed using MALDI-TOF/TOF (Figure 5B). Our analysis revealed that upon limited proteolysis hIL-34$_{FL}$ in the hIL-34$_{FL}$:hCSF-1R$_{D1-D5}$ complex is truncated at its C terminus to yield hIL-34$_{TRUNC}$. Furthermore, hCSF-1R$_{D1-D5}$ loses the entire D5. To investigate the intactness of the native N termini in hIL-34$_{TRUNC}$ and hCSF-1R$_{TRUNC}$, we performed Edman degradation (Figure 5C), which confirmed that both native N termini were present. We also measured the molecular (MW) of hIL-34$_{FL}$ by linear mode MALDI-TOF analysis, revealing a MW of approximately 31 kDa for the fully glycosylated protein. Such MW differs by 5 kDa from the theoretical MW of 26 kDa. As O-glycosylation in HEK293 cells was recently shown to be of the GalNAc-NeuNAc-Gal-NeuNAc type (Geoghegan et al., 2013), we can deduce that at least five O-linked glycans must be present in the C-terminal segment of hIL-34$_{FL}$.

Our findings confirm that the C terminus of hIL-34$_{FL}$ is heavily glycosylated via O-linked glycans, providing insights into the already observed differences between IL-34 and CSF-1 in terms of functionality and signaling activation patterns (Chihara et al., 2010). Indeed, O-glycosylation in signaling molecules plays a role in protein stability, clearance, and/or modulation of its signaling activity (Van den Steen et al., 1998). Interestingly, O-glycosylation of the mucin type (O-GalNAc) preferentially occurs in inherently disordered regions (Nishikawa et al., 2010). We envisage that our findings will stimulate further research on the dissection of glycosylation in the C-terminal tail of IL-34 and its functional role.

DISCUSSION

The discovery of IL-34 as a second cytokine ligand for hematopoietic CSF-1R has raised intriguing structural and mechanistic questions as to how two cytokines with unidentifiable sequence homology might activate the same cognate receptor. This has also created a potential avenue to shed light into the

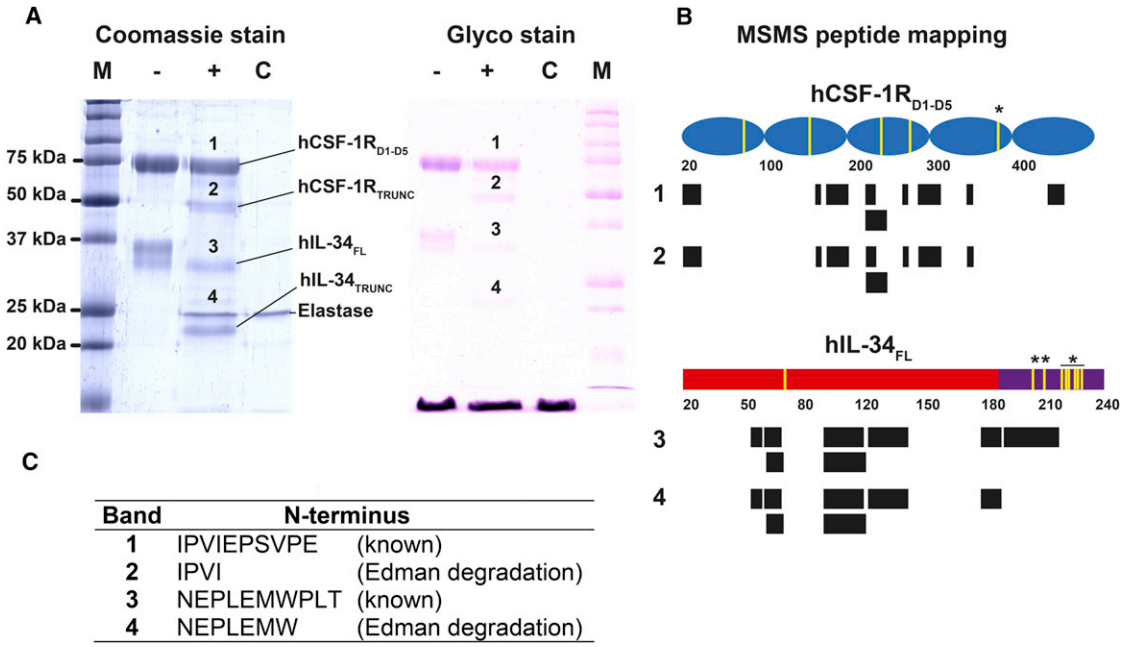

Band	N-terminus	
1	IPVIEPSVPE	(known)
2	IPVI	(Edman degradation)
3	NEPLEMWPLT	(known)
4	NEPLEMW	(Edman degradation)

Figure 5. Limited Proteolysis of the hIL-34$_{FL}$:hCSF1-R$_{D1-D5}$ Complex followed by SDS-PAGE Analysis, MALDI-TOF/TOF MSMS Analysis, and Edman Degradation

(A) SDS-PAGE analysis of hIL-34$_{FL}$:hCSF1-R$_{D1-D5}$ after incubation with elastase at 24°C. Gels were run in duplicate and stained by Coomassie blue (left) and glycostaining (right). Lane 1, marker (M); lane 2, hIL-34$_{FL}$:hCSF1-R$_{D1-D5}$ before cleavage (−); lane 3, hIL-34$_{FL}$:hCSF1-R$_{D1-D5}$ after 2.5 hr incubation with elastase (+); and lane 4, elastase (C, control). While forming a complex, both hCSF-1R$_{D1-D5}$ (band 1, 75 kDa) and hIL-34$_{FL}$ (band 3, 37 kDa) can be truncated to species of lower MW (labeled as hCSF-1R$_{TRUNC}$, band 2, 50 kDa, and hIL-34$_{TRUNC}$, band 4, 23 kDa). In the case of hIL-34$_{FL}$, truncation results in an almost complete loss of glycostain signal.

(B) MALDI-TOF/TOF analysis of hCSF1-R$_{D1-D5}$ (1), hCSF-1R$_{TRUNC}$ (2), hIL-34$_{FL}$ (3), and hIL-34$_{TRUNC}$ (4) bands cut from a Coomassie-stained SDS-PAGE gel. Peptides identified by mass spectrometry are shown as black boxes and are mapped on hCSF-1R$_{D1-D5}$ (blue) and hIL-34$_{FL}$ (red, predicted unstructured region in purple). Glycans structurally confirmed by crystallographic data (Ma et al., 2012) are shown as yellow lines. Predicted glycans, using the netNglyc server for N-linked glycans (Gupta et al., 2004) and the netOglyc server for O-linked glycans (Julenius et al., 2005), are marked by an asterisk. See also Table S2.

(C) Edman degradation of truncated hIL-34$_{FL}$ and hCSF-1R$_{D1-D5}$ after incubation with elastase. Identified N termini for hIL-34$_{TRUNC}$ and hCSF-1R$_{TRUNC}$ are identical to the native N termini of hIL-34$_{FL}$ and hCSF-1R$_{D1-D5}$.

mechanistic requirements of CSF-1R activation and, by extrapolation, that of other homologous RTK-III family members. This is particularly opportune in light of the recent tremendous progress in our understanding of the assembly principles of extracellular RTK-III with cognate cytokines and their impact on rationalizing RTK-III evolution and role in cancer and inflammation (Verstraete and Savvides, 2012).

In this study, we have built upon recent structural work dissecting IL-34 and CSF-1 complexes with CSF-1R to provide the missing link toward a possible consensus of the activation principles of CSF-1R (Chen et al., 2008; Elegheert et al., 2011; Liu et al., 2012; Ma et al., 2012). Structural studies thus far have elucidated the structure of human and mouse IL-34 and provided details of the IL-34 interaction epitope on CSF-1R accommodated by a grapple formed by the CSF-1R$_{D2-D3}$ module (Liu et al., 2012; Ma et al., 2012). A comparison of the mIL-34 and mCSF-1 interaction sites on mouse CSF-1R reveals coverage of the same general footprint but with distinct interactions in each case (Liu et al., 2012). Such detailed comparison of interaction epitopes is not yet available for the human counterparts because of the absence of a high-resolution structure for the human CSF-1:CSF-1R complex.

Our hybrid structural analysis combining SAXS and EM studies of full-length human IL-34 and a functional truncation mutant thereof lacking 50 amino acids at the C terminus, in complex with the full-length hCSF-1R ectodomain, has sought to provide insights into the structural role of the membrane-proximal domains D4 and D5 in CSF-1R in complex formation and to provide views of the complete extracellular complexes. In addition, we interrogated the structural role of the C-terminal segment of IL-34 in complex formation and investigated its biochemical properties.

Our structural studies have shown that dimerization of CSF-1R by IL-34 evokes receptor-receptor contacts between adjacent membrane-proximal D4 domains in CSF-1R, while D1 and D5 extend away from the core of the complex. Importantly, the IL-34:CSF-1R extracellular assembly is strikingly similar in geometry and molecular principles employed to the CSF-1:CSF-1R complex (Elegheert et al., 2011). The biological implications of these observations are profound because they now allow us, in conjunction with the plethora of structural and biochemical studies of CSF-1 and IL-34 interactions with cognate and noncognate CSF-1R (Chen et al., 2008; Elegheert et al., 2011, 2012; Lin et al., 2008; Liu et al., 2012; Ma et al., 2012), to establish a consensus for the assembly of signaling

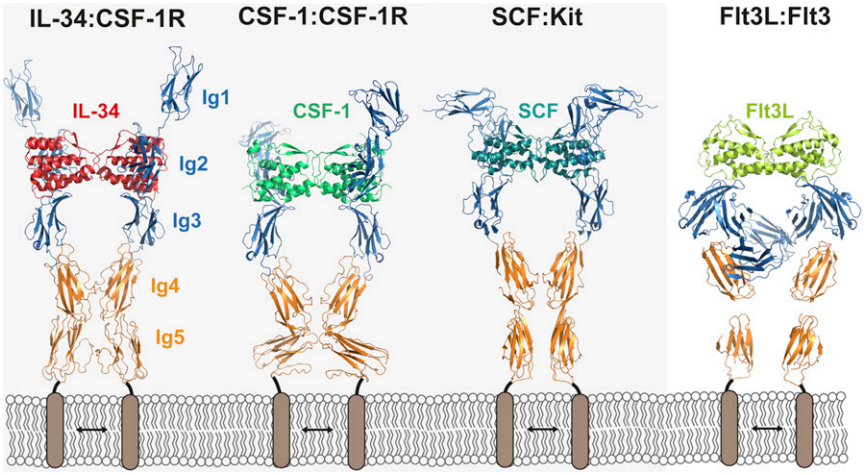

Figure 6. Overview of RTKIII Full Ectodomain Complexes with Cognate Cytokines
Left: solution SAXS structure of the IL-34:CSF-1R complex. Middle left: solution SAXS structure of the CSF-1:CSF-1R complex. Middle right: crystal structure of the SCF:Kit complex (PDB ID code 2E9W). Right: crystal structure of the Flt3L:Flt3 complex (PDB ID code 3QS9). Transmembrane helix regions of opposing receptors are shown as rectangular blocks in gray. Not shown are the intracellular split-kinase domains of the receptors, which become phosphorylated upon cytokine-induced receptor dimerization.

complexes of CSF-1R by two distinct cytokine ligands. In the first instance, dimeric CSF-1 and IL-34 each offer specific receptor binding sites leading to initial ternary complexes targeting the D2-D3 modules of CSF-1R (Chen et al., 2008; Elegheert et al., 2011; Liu et al., 2012; Ma et al., 2012). This initial complex primes homotypic receptor interactions in dimerized CSF-1R between conserved sequence fingerprints localized in CSF-1R_{D4} to drive assembly of a cooperative high-affinity complex (Elegheert et al., 2011). We note that equivalent receptor homotypic interactions have been confirmed in the homologous KIT (Yuzawa et al., 2007) and PDGFRβ (Yang et al., 2008), and in VEGFR (Kisko et al., 2011; Ruch et al., 2007; Yang et al., 2010), from the related RTK-V family. With the exception of Flt3, all RTK-III and RTK-V members carry a conserved dimerization sequence fingerprint in D4 or D7 (Verstraete et al., 2011b). Recent studies employing an engineered monomeric variant of hCSF-1, dimeric hCSF-1, and truncation ectodomain variants of hCSF-1R have deconvoluted the positive cooperativity of hCSF-1:hCSF-1R complexes into modular contributions stemming from an initial encounter complex (with low μM affinity), the dimer plasticity of hCSF-1 (contributing one order of magnitude to the K_D), and receptor ectodomain contacts at the level of D4 (improving the K_D by 1-2 orders of magnitude) (Elegheert et al., 2012). Whereas such detailed studies are not yet available for IL-34, binding studies have already shown that the membrane-proximal domains in CSF-1R contribute at least one order of magnitude to the affinity of the extracellular complex (Liu et al., 2012; Ma et al., 2012). Furthermore, hIL-34 displays plasticity in its dimeric assembly as shown via the structure of its complex with Fab fragments (Ma et al., 2012). Such structural plasticity has already been observed in all other helical cytokines activating RTK-III (Elegheert et al., 2012; Verstraete et al., 2011b; Yuzawa et al., 2007) and has been proposed as a common mechanistic element of RTK-III activation (Verstraete and Savvides, 2012).

The advent of a structural view of the complete IL-34:CSF-1R extracellular complex has essentially brought the spectrum of full-length ectodomain complexes of RTK-III with helical cytokines to full circle (Figure 6). This collection of structures now provides the most direct evidence to date that similarly sized dimeric helical cytokine ligands of RTK-III evolved to respond to conserved geometric requirements for the productive alignment of membrane proximal D4 and D5, thereby coupling cytokine binding to intracellular activation of the RTK-III kinase domains (Verstraete and Savvides, 2012). We note in particular that the consensus feature in all four RTK-III cytokines is their ability to bind to D3 of their cognate RTK-III receptors, bringing the dimerized receptor molecules within a critical distance of ~60 Å. IL-34 and CSF-1 offer perhaps the best evidence for this mechanistic principle. Despite their greatly divergent sequences, IL-34 and CSF-1 establish strikingly similar extracellular assemblies with their common receptor, CSF-1R (Figures 1 and 6), and appear to have evolved to meet the activation requirements of CSF-1R. We envisage that such insights may impact therapeutic targeting of RTK-III, as efforts are beginning to shift toward combined approaches, focusing both in the intracellular kinase domains and the receptor ectodomains (Verstraete and Savvides, 2012).

EXPERIMENTAL PROCEDURES

Production of Recombinant Human IL-34 and IL-34:CSF-1R Complexes

Constructs, including coding sequences of full-length (hIL-34_{FL}, residues N21-P242) and truncated (hIL-$34_{N21-P200}$, residues N21-P200) human interleukin 34, each containing a C-terminal His_6-tag, were cloned into the pcDNA4TO vector (Invitrogen, Carlsbad, CA, USA). Human colony stimulating factor 1 receptor ectodomains 1-3 (hCSF-$1R_{D1-D3}$) and 1-5 (hCSF-$1R_{D1-D5}$) constructs containing C-terminal His_6-tags were cloned into the pHLsec vector (Aricescu et al., 2006). We used HEK293S GnTI$^{-/-}$ cells (Reeves et al., 2002; Verstraete et al., 2011a), which lack N-acetylglucosaminyltransferase-I, to establish stable tetracycline-inducible cell lines expressing hIL-34_{FL} and hIL-$34_{N21-P200}$ with homogeneous $GlcNAc_2Man_5$ N-glycans. Because of aggregation of unbound hIL-34, a coexpression protocol was established in which hCSF-$1R_{D1-D3}$ and hCSF-$1R_{D1-D5}$ ectodomain constructs were transiently transfected (Aricescu et al., 2006; Chang et al., 2007) into the stable cell lines expressing hIL-34_{FL} and hIL-$34_{N21-P200}$. During transfection, tetracycline and sodium butyrate were added to the transfection medium to ensure coexpression of both ligand and receptor. Expression medium was harvested after 5 days of expression and always contained the complex of interest (hIL-$34_{N21-P200}$:hCSF-$1R_{D1-D3}$, hIL-$34_{N21-P200}$: hCSF- $1R_{D1-D5}$, or hIL-34_{FL}: hCSF-$1R_{D1-D5}$), together with an excess of receptor (hCSF-$1R_{D1-D3}$ or hCSF-$1R_{D1-D5}$), which always expressed at higher levels than IL-34. Target complexes were purified by immobilized metal affinity chromatography using a Co^{2+}-loaded TALON FF column (Clontech, Mountain View, CA, USA). Next, eluted fractions were pooled and injected onto a Prep-Grade Hiload 16/60 SD-200 column (GE Healthcare, Waukesha, WI, USA). Peak fractions corresponding to hIL-$34_{N21-P200}$:hCSF-$1R_{D1-D3}$, hIL-$34_{N21-P200}$:hCSF-$1R_{D1-D5}$, or

hIL-34_{FL}:hCSF-$1R_{D1-D5}$ complexes were pooled and used for the MALLS, SAXS, and EM experiments described further.

Multiangle Laser Light Scattering

Determination of the molecular masses of hIL-$34_{N21-P200}$:hCSF-$1R_{D1-D3}$, hIL-$34_{N21-P200}$:hCSF-$1R_{D1-D5}$, and hIL-34_{FL}:hCSF-$1R_{D1-D5}$ complexes was performed by MALLS. Protein samples were injected into a high-pressure liquid chromatography (HPLC)- (Shimadzu, Kyoto, Japan) FFF module (Wyatt Technology, Goleta, CA, USA) equilibrated with a 20 mM HEPES (pH 7.5) and 150 mM NaCl buffer. The FFF module was coupled to an online UV detector (Shimadzu), an 18-angle light scattering detector (DAWN HELEOS), and a refractive index detector (Optilab T-rEX) (Wyatt Technology). Protein concentrations used were in the 1–10 mM range. An refractive index (RI) increment value (dn/dc value) of 0.185 ml/g was used for the protein concentration and molecular mass determination. FFF cross-flows were varied to optimize the resolution of separation. Data analysis were carried out using the ASTRA V software.

Small-Angle X-Ray Scattering

SAXS data were collected at the European Molecular Biology Laboratory - X33 beamline on the storage ring DORIS III at Deutsches Elektronen-Synchrotron (DESY, Hamburg) (Blanchet et al., 2012; Roessle et al., 2007) and the ID 14-3 beamline at European Synchrotron Radiation Facility (ESRF, Grenoble) (Pernot et al., 2010). Measurements were carried out at 283 K (X33) or 293 K (ID-14-3), within a momentum transfer range of 0.01 $Å^{-1} < s < 0.6\ Å^{-1}$, where $s = 4\pi\sin(\theta)/\lambda$ and 2θ is the scattering angle. Samples were measured at solute concentrations of 1.5, 3.5, and 5 mg/ml in 50 mM Na_2HPO4 (pH 7.5) and 100 mM NaCl for hIL-$34_{N21-P200}$:hCSF-$1R_{D1-D3}$. hIL-$34_{N21-P200}$:hCSF-$1R_{D1-D5}$ and hIL-34_{FL}:hCSF-$1R_{D1-D5}$ samples were recuperated from the MALLS experiments described earlier and subsequently concentrated to 1, 2, and 3 mg/ml (hIL-$34_{N21-P200}$:hCSF-$1R_{D1-D5}$) or 0.5, 1, and 3 mg/ml (hIL-34_{FL}:hCSF-$1R_{D1-D5}$) in 20 mM HEPES (pH 7.5) and 150 mM NaCl. No measurable radiation damage was detected on comparison of eight (X33) or ten (ID14-3) successive time frames with 15 s (X33) or 10 s (ID-14-3) exposures. Initial data processing were performed at the beamlines using automatic protocols developed at EMBL Hamburg (Franke et al., 2012). Buffer subtraction and extrapolation to infinite dilution were performed by the program PRIMUS (Konarev et al., 2003) in accordance with standard procedures. Merged curves were generated using the low angle part of the lowest concentration curve and the high angle part of the highest concentration curve. The Guinier region was evaluated by PRIMUS using Guinier approximation (Guinier, 1939). The Porod volume was evaluated using PRIMUS. The radius of gyration r_g, forward scattering I_0, maximum particle dimension D_{max}, and the distance distribution function $P(r)$ were evaluated using GNOM (Svergun, 1992). Molecular masses of different constructs were calculated by comparison with the reference BSA sample. Theoretical scattering patterns from available structures and generated models, together with their respective discrepancy to the experimental data, were calculated using CRYSOL (Petoukhov et al., 2012; Svergun et al., 1995).

Ab Initio Modeling of SAXS Data

Ab initio shape reconstructions were performed using the bead modeling programs DAMMIF (Franke and Svergun, 2009) for hIL-$34_{N21-P200}$:hCSF-$1R_{D1-D5}$ and DAMMIN (Svergun, 1999) for hIL-$34_{N21-P200}$:hCSF-$1R_{D1-D3}$. Both DAMMIF and DAMMIN were run ten times, imposing 2-fold symmetry. The generated DAMMIF and DAMMIN models were subsequently averaged with application of P2 symmetry, using the DAMAVER program suite (Volkov and Svergun, 2003).

Rigid-Body Modeling of SAXS Data

The online version of SASREF (Petoukhov et al., 2012; Petoukhov and Svergun, 2005) was used to perform rigid-body refinements of the hIL-$34_{N21-P200}$:hCSF-$1R_{D1-D3}$, hIL-$34_{N21-P200}$:hCSF-$1R_{D1-D5}$, and hIL-34_{FL}:hCSF-$1R_{D1-D5}$ complexes. In each case, data up to 0.25 $Å^{-1}$ was used and P2 symmetry was imposed. For both hIL-$34_{N21-P200}$:hCSF-$1R_{D1-D3}$ and hIL-$34_{N21-P200}$:hCSF-$1R_{D1-D5}$, the crystal structure of hIL-34 bound to hCSF-$1R_{D2-D3}$ was taken (Ma et al., 2012) (Protein Data Bank [PDB] ID code 4DKD) as one rigid body, whereas D1 was allowed to move with a contact restraint of 5 Å between its C terminus and the N terminus of hCSF-$1R_{D2-D3}$. Five $GlcNAc_2Man_5$ N-glycans, treated as rigid bodies, were added to the model with contact restraints of 5 Å to truncated asparagine residues N75 on hIL-34 and N73, N153, N240, and N275 of hCSF-$1R_{D1-D3}$. The C-atoms of these N-glycans were changed to Cα-atoms to prevent clashes during SASREF runs. The native glycosylation state of the hIL-34:hCSF-$1R_{D1-D3}$ complex was inferred from the hIL-34:hCSF-$1R_{D1-D3}$ structure (Ma et al., 2012). For the hIL-$34_{N21-P200}$:hCSF-$1R_{D1-D5}$ SASREF runs, 3D models for hCSF-$1R_{D4}$ and hCSF-$1R_{D5}$ were generated using the online version of I-Tasser (Roy et al., 2010). These models were made using D4 and D5 of the KIT receptor (Yuzawa et al., 2007) as respective templates, with a sequence identity/coverage of 30%/97% and 30%/90%, respectively. Ambiguous contact distances between D4 and D4' were imposed based on the structure of the SCF:KIT complex (PDB ID code 2E9W) and the conserved Arg-Glu motive present in the hCSF-$1R_{D4}$ sequence. Finally, an extra N-glycan was added to N353 of hCSF-$1R_{D4}$, based on an N-glycosylation prediction performed by the netNglyc server (Gupta et al., 2004). The same approach was used to reanalyze SAXS data from a previous study on hCSF-1:hCSF-1R complexes (Elegheert et al., 2011). Rigid-body runs were carried out using the online version of SASREF. The same set of rigid bodies and contact restraints (including glycans on N73, N153, N240, N275, and N353 of hCSF-$1R_{D1-D5}$) was used as described for hIL-$34_{N21-P200}$:hCSF-$1R_{D1-D5}$, except for the replacement of hIL-34:hCSF-$1R_{D2-D3}$ with mCSF-1:mCSF-$1R_{D2-D3}$ taken from PDB ID code 3EJJ (Chen et al., 2008). V153, G240, and I275 of mCSF-$1R_{D2-D3}$ were truncated to C_α during SASREF runs and afterward mutated to asparagine residues to provide identical glycosylation spots as found in hCSF-$1R_{D2-D3}$.

Energy Minimization of SASREF Rigid-Body Models

To obtain structures that were as chemically correct as possible, missing residues and gaps present in the SASREF rigid-body models were added, and physical linkages were made between glycosylated asparagine residues and their GlcNAc sugars, followed by a round of energy minimization. All-atom simulations were conducted using NAMD 2.8 (Phillips et al., 2005), relying on the CHARMM force field (Guvench et al., 2008, 2009, 2011; MacKerell et al., 1998; Mackerell et al., 2004). Additional parameters were introduced to describe the asparagine-GlcNAc linkage, by analogy to existing parameters (see Table S3). Topologies and initial structures were constructed with VMD (Humphrey et al., 1996) based on the structures obtained from SASREF refinement. Missing loops were modeled using FREAD (Choi and Deane, 2010). Resulting all-atom structures were then energy minimized in a stepwise fashion, each time doing 5,000 minimization steps, while gradually lifting constraints. First, all GlcNAc glycan moieties and amino acids in modeled loops were unrestrained, while position restraints were applied to all other atoms (with a harmonic force constant of 5 kcal/mol/$Å^2$). Subsequently, position restraints were only applied to mannose residues along with a distance restraint (5.2 Å with a harmonic force constant of 10 kcal/mol/$Å^2$) on the salt bridges between E76 and R72 of opposing hCSF-$1R_{D4}$ chains. In the next steps, these constraints were lifted, first by 10-fold reduction of the force constant and then by turning off constraints all together, finalizing by a 5,000-step minimization without constraints. All simulations were done with a generalized Born implicit solvent model of water (Tanner et al., 2011). Finally, CRYSOL was used to calculate scattering patterns of the energy-minimized SASREF models and their discrepancy to the experimental SAXS data. No significant changes in respective χ^2 values were detected after addition of missing loops and energy minimization of the SASREF models. χ^2 values presented in Figures 2, 3, and 4 and Table S1 represent the χ^2 values after energy minimization.

Negative Stain Electron Microscopy

For preparation of negatively stained hIL34$_{FL}$:hCSF-$1R_{D1-D5}$ complex, purified sample with a concentration of 0.1 mg/ml in HEPES buffer (20 mM HEPES and 150 mM NaCl [pH 7.4]) was applied to the clear side of carbon on a carbon-mica interface and stained with Nano-W from nanoprobes. Images were recorded under low-dose conditions with a JEOL 1200 EX II microscope at 100 kV and at a 52,974x magnification with an Orius SC600 Gatan CCD camera. Images were binned to a pixel size of 3.4 Å at the object scale. A data set of circa 12,000 96*96 pixel subframes was semiautomatically selected

with the boxer routine of EMAN (Ludtke et al., 1999), CTF-corrected with CTFFIND3 (Mindell and Grigorieff, 2003), and bsoft (Heymann et al., 2008) and low-pass-filtered at 15 Å resolution. The translationally centered data set was subjected to multivariate statistical analysis (MSA) and classification with Imagic-5 (van Heel et al., 1996). Characteristic class averages with the best overall quality were used as a set of references for multireference alignment followed by MSA and classification. After several iterations and obtainment of stable classes, the inside of each class of individual frames was sorted according to the correlation with the respective class average, and the fifty best subframes of each class were summed up into a second reference used for realignment and production of improved class averages. These class averages were aligned against projections of the SAXS model of the hIL-$34_{N21-P200}$:hCSF-$1R_{D1-D5}$ complex filtered to 30 Å resolution for visual comparison.

Limited Proteolysis, Edman Degradation, and MALDI-TOF/TOF MSMS Analysis

For the limited proteolysis experiments, 43 μl of hIL-34_{FL}:hCSF-$1R_{D1-D5}$ (0.1 mg/ml in 20 mM HEPES and 150 mM NaCl [pH 7.5]) was mixed with 2 μl elastase (Sigma-Aldrich, St. Louis, MO, USA; 500 μg/ml in 0.1 M Tris-HCl [pH 8]) and 5 μl 10X protease buffer (1 M Tris-HCl [pH 8]). Proteolysis was carried out at 24°C and was stopped after 2.5 hr by boiling at 95°C for 10 min after addition of Laemmli buffer and β-mercaptoethanol. The experiment was run in duplicate and analyzed using SDS-PAGE followed by Coomassie staining and glycostaining (Pierce Glycoprotein Staining Kit, Thermo Scientific, Waltham, MA, USA), respectively.

Coomassie-stained bands were cut out and digested with trypsin and/or chymotrypsin (Promega, Madison, WI, USA) overnight at 37°C. The next day, peptides were extracted by adding 40 μl 60% acetonitrile/0.1% HCOOH to the gel pieces. After drying of the peptide mixture, peptides were redissolved in 10 μl 0.1% formic acid, mixed with 3 mg/ml α-cyano hydroxycinnamic acid (Sigma-Aldrich) in 50% acetonitrile/0.1% TFA, and analyzed by mass spectrometry using a 4800 plus TOF/TOF analyzer (Applied Biosystems, Foster City, CA, USA). N-terminal sequence determination of equivalent bands was performed by automated Edman degradation on a Procise model 494 sequencer instrument, equipped with an on-line HPLC system consisting of a 140C Microgradient pump and a 785A programmable absorbance detector (all from Applied Biosytems). The analysis was performed with acid delivery in the gas phase after electroblotting the protein sample to a polyvinylidene difluoride membrane (Applied Biosystems). Intact protein analysis of purified hIL-34_{FL} in phosphate buffer (50 mM Na_2HPO_4 and 300 mM NaCl) was performed using a 4800 plus TOF/TOF analyzer (Applied Biosystems) acting in linear mode. To improve ionization, the sample was diluted 10-fold in 0.1% formic acid and directly spotted on a MALDI target plate.

SUPPLEMENTAL INFORMATION

Supplemental Information includes three figures and three tables and can be found with this article online at http://dx.doi.org/10.1016/j.str.2013.01.018.

ACKNOWLEDGMENTS

We thank the European Synchrotron Radiation Facility (ESRF) and DESY/EMBL for synchrotron beam time allocation and the staff of beamlines ID14-3 (ESRF) and X33 (DESY/EMBL) for technical support. Access to these synchrotron facilities is supported by the European Commission under the 7th Framework Programme: Research Infrastructures, Grant Agreement Number 226716. This research project was supported by grants from the Research Foundation Flanders (FWO) (3G064307, G059710, and G0B7912N) and Ghent University (BOF instrument) to S.N.S., a Ghent University cofinancing grant to Y.W. and B.D., and a Bundesministerium für Bildung und Forschung (BMBF) research grant Sync-Life (contract: 05K10YEA) to D.I.S. I.G. thanks the EM platform of the Partnership for Structural Biology (Grenoble) for access to EM equipment. J.F., J.E., E. Pauwels, and B.V. were supported by research fellowships from the FWO. Y.W. is supported by a research fellowship from the Chinese Scholarship Council (CSC). The computational resources and services used were provided by Ghent University (Stevin Supercomputer Infrastructure). J.F., J.E., N.B., and E. Pannecoucke expressed and purified recombinant proteins. Y.W, I.V.B, and B.D. carried out mass spectrometry and N-terminal sequencing of peptides. J.F. carried out limited proteolysis experiments with contributions from B.V. and E. Pannecoucke. J.F. carried out all structural analyses with contributions from J.E., E. Pauwels, and S.N.S. J.F. and E. Pauwels carried out molecular dynamics calculations. J.F., J.E., A.S., and D.S. carried out SAXS measurements. I.G. carried out EM imaging and data analysis. J.F., B.V., and S.N.S. established the experimental approach and designed experiments. S.N.S. directed the study. J.F. and S.N.S. wrote the manuscript with contributions from all authors.

Received: November 22, 2012
Revised: January 22, 2013
Accepted: January 28, 2013
Published: March 7, 2013

REFERENCES

Alt, A., Miguel-Romero, L., Donderis, J., Aristorena, M., Blanco, F.J., Round, A., Rubio, V., Bernabeu, C., and Marina, A. (2012). Structural and functional insights into endoglin ligand recognition and binding. PLoS ONE *7*, e29948.

Aricescu, A.R., Lu, W., and Jones, E.Y. (2006). A time- and cost-efficient system for high-level protein production in mammalian cells. Acta Crystallogr. D Biol. Crystallogr. *62*, 1243–1250.

Baud'huin, M., Renault, R., Charrier, C., Riet, A., Moreau, A., Brion, R., Gouin, F., Duplomb, L., and Heymann, D. (2010). Interleukin-34 is expressed by giant cell tumours of bone and plays a key role in RANKL-induced osteoclastogenesis. J. Pathol. *221*, 77–86.

Blanchet, C.E., Zozulya, A.V., Kikhney, A.G., Franke, D., Konarev, P.V., Shang, W., Klaering, R., Robrahn, B., Hermes, C., Cipriani, F., et al. (2012). Instrumental setup for high-throughput small- and wide-angle solution scattering at the X33 beamline of EMBL Hamburg. J. Appl. Cryst. *45*, 489–495.

Chang, V.T., Crispin, M., Aricescu, A.R., Harvey, D.J., Nettleship, J.E., Fennelly, J.A., Yu, C., Boles, K.S., Evans, E.J., Stuart, D.I., et al. (2007). Glycoprotein structural genomics: solving the glycosylation problem. Structure *15*, 267–273.

Chen, X., Liu, H., Focia, P.J., Shim, A.H.-R., and He, X. (2008). Structure of macrophage colony stimulating factor bound to FMS: diverse signaling assemblies of class III receptor tyrosine kinases. Proc. Natl. Acad. Sci. USA *105*, 18267–18272.

Chihara, T., Suzu, S., Hassan, R., Chutiwitoonchai, N., Hiyoshi, M., Motoyoshi, K., Kimura, F., and Okada, S. (2010). IL-34 and M-CSF share the receptor Fms but are not identical in biological activity and signal activation. Cell Death Differ. *17*, 1917–1927.

Chitu, V., and Stanley, E.R. (2006). Colony-stimulating factor-1 in immunity and inflammation. Curr. Opin. Immunol. *18*, 39–48.

Choi, Y., and Deane, C.M. (2010). FREAD revisited: accurate loop structure prediction using a database search algorithm. Proteins *78*, 1431–1440.

Dai, X.-M., Ryan, G.R., Hapel, A.J., Dominguez, M.G., Russell, R.G., Kapp, S., Sylvestre, V., and Stanley, E.R. (2002). Targeted disruption of the mouse colony-stimulating factor 1 receptor gene results in osteopetrosis, mononuclear phagocyte deficiency, increased primitive progenitor cell frequencies, and reproductive defects. Blood *99*, 111–120.

Elegheert, J., Desfosses, A., Shkumatov, A.V., Wu, X., Bracke, N., Verstraete, K., Van Craenenbroeck, K., Brooks, B.R., Svergun, D.I., Vergauwen, B., et al. (2011). Extracellular complexes of the hematopoietic human and mouse CSF-1 receptor are driven by common assembly principles. Structure *19*, 1762–1772.

Elegheert, J., Bracke, N., Pouliot, P., Gutsche, I., Shkumatov, A.V., Tarbouriech, N., Verstraete, K., Bekaert, A., Burmeister, W.P., Svergun, D.I., et al. (2012). Allosteric competitive inactivation of hematopoietic CSF-1 signaling by the viral decoy receptor BARF1. Nat. Struct. Mol. Biol. *19*, 938–947.

Franke, D., and Svergun, D.I. (2009). *DAMMIF*, a program for rapid *ab-initio* shape determination in small-angle scattering. J. Appl. Cryst. *42*, 342–346.

Franke, D., Kikhney, A.G., and Svergun, D.I. (2012). Automated acquisition and analysis of small angle X-ray scattering data. Nucl. Instr. Meth. Phys. Res. A *689*, 52–59.

Garceau, V., Smith, J., Paton, I.R., Davey, M., Fares, M.A., Sester, D.P., Burt, D.W., and Hume, D.A. (2010). Pivotal advance: avian colony-stimulating factor 1 (CSF-1), interleukin-34 (IL-34), and CSF-1 receptor genes and gene products. J. Leukoc. Biol. *87*, 753–764.

Geoghegan, K.F., Song, X., Hoth, L.R., Feng, X., Shanker, S., Quazi, A., Luxenberg, D.P., Wright, J.F., and Griffor, M.C. (2013). Unexpected mucin-type O-glycosylation and host-specific N-glycosylation of human recombinant interleukin-17A expressed in a human kidney cell line. Protein Expr. Purif. *87*, 27–34.

Gow, D.J., Garceau, V., Kapetanovic, R., Sester, D.P., Fici, G.J., Shelly, J.A., Wilson, T.L., and Hume, D.A. (2012a). Cloning and expression of porcine Colony Stimulating Factor-1 (CSF-1) and Colony Stimulating Factor-1 Receptor (CSF-1R) and analysis of the species specificity of stimulation by CSF-1 and Interleukin 34. Cytokine *60*, 793–805.

Gow, D.J., Garceau, V., Pridans, C., Gow, A.G., Simpson, K.E., Gunn-Moore, D., and Hume, D.A. (2012b). Cloning and expression of porcine colony stimulating factor-1 (CSF-1) and colony stimulating factor-1 Receptor (CSF-1R) and analysis of the species specificity of stimulation by CSF-1 and Interleukin 34. Cytokine *60*, 793–805.

Greter, M., Lelios, I., Pelczar, P., Hoeffel, G., Price, J., Leboeuf, M., Kündig, T.M., Frei, K., Ginhoux, F., Merad, M., and Becher, B. (2012). Stroma-derived interleukin-34 controls the development and maintenance of langerhans cells and the maintenance of microglia. Immunity *37*, 1050–1060.

Guinier, A. (1939). La diffraction des rayons X aux tres petits angles: applications a l'etude de phenomenes ultramicroscopiques. Ann. Phys. (Paris) *12*, 161–237.

Gupta, R., Jung, E., and Brunak, S. (2004). Prediction of N-glycosylation sites in human proteins. http://wwwcbsdtudk/services/NetNGlyc/.

Guttman, M., Kahn, M., Garcia, N.K., Hu, S.-L., and Lee, K.K. (2012). Solution structure, conformational dynamics, and CD4-induced activation in full-length, glycosylated, monomeric HIV gp120. J. Virol. *86*, 8750–8764.

Guvench, O., Greene, S.N., Kamath, G., Brady, J.W., Venable, R.M., Pastor, R.W., and Mackerell, A.D., Jr. (2008). Additive empirical force field for hexopyranose monosaccharides. J. Comput. Chem. *29*, 2543–2564.

Guvench, O., Hatcher, E.R., Venable, R.M., Pastor, R.W., and Mackerell, A.D. (2009). CHARMM additive all-atom force field for glycosidic linkages between hexopyranoses. J. Chem. Theory Comput. *5*, 2353–2370.

Guvench, O., Mallajosyula, S.S., Raman, E.P., Hatcher, E., Vanommeslaeghe, K., Foster, T.J., Jamison, F.W., 2nd, and Mackerell, A.D., Jr. (2011). CHARMM additive all-atom force field for carbohydrate derivatives and its utility in polysaccharide and carbohydrate-protein modeling. J. Chem. Theory Comput. *7*, 3162–3180.

Hamilton, J.A., and Achuthan, A. (2012). Colony stimulating factors and myeloid cell biology in health and disease. Trends Immunol. *34*, 81–89.

Heymann, J.B., Cardone, G., Winkler, D.C., and Steven, A.C. (2008). Computational resources for cryo-electron tomography in Bsoft. J. Struct. Biol. *161*, 232–242.

Humphrey, W., Dalke, A., and Schulten, K. (1996). VMD: visual molecular dynamics. J. Mol. Graph. *14*, 33–38, 27–28.

Julenius, K., Mølgaard, A., Gupta, R., and Brunak, S. (2005). Prediction, conservation analysis, and structural characterization of mammalian mucin-type O-glycosylation sites. Glycobiology *15*, 153–164.

Kajander, T., Kuja-Panula, J., Rauvala, H., and Goldman, A. (2011). Crystal structure and role of glycans and dimerization in folding of neuronal leucine-rich repeat protein AMIGO-1. J. Mol. Biol. *413*, 1001–1015.

Kisko, K., Brozzo, M.S., Missimer, J., Schleier, T., Menzel, A., Leppänen, V.-M., Alitalo, K., Walzthoeni, T., Aebersold, R., and Ballmer-Hofer, K. (2011). Structural analysis of vascular endothelial growth factor receptor-2/ligand complexes by small-angle X-ray solution scattering. FASEB J. *25*, 2980–2986.

Konarev, P.V., Volkov, V.V., Sokolova, A.V., Koch, M.H.J., and Svergun, D.I. (2003). *PRIMUS*: a Windows PC-based system for small-angle scattering data analysis. J. Appl. Cryst. *36*, 1277–1282.

Lemmon, M.A., and Schlessinger, J. (2010). Cell signaling by receptor tyrosine kinases. Cell *141*, 1117–1134.

Lin, H., Lee, E., Hestir, K., Leo, C., Huang, M., Bosch, E., Halenbeck, R., Wu, G., Zhou, A., Behrens, D., et al. (2008). Discovery of a cytokine and its receptor by functional screening of the extracellular proteome. Science *320*, 807–811.

Liu, H., Leo, C., Chen, X., Wong, B.R., Williams, L.T., Lin, H., and He, X. (2012). The mechanism of shared but distinct CSF-1R signaling by the non-homologous cytokines IL-34 and CSF-1. Biochim. Biophys. Acta *1824*, 938–945.

Ludtke, S.J., Baldwin, P.R., and Chiu, W. (1999). EMAN: semiautomated software for high-resolution single-particle reconstructions. J. Struct. Biol. *128*, 82–97.

Ma, X., Lin, W.Y., Chen, Y., Stawicki, S., Mukhyala, K., Wu, Y., Martin, F., Bazan, J.F., and Starovasnik, M.A. (2012). Structural basis for the dual recognition of helical cytokines IL-34 and CSF-1 by CSF-1R. Structure *20*, 676–687.

Mackerell, A.D., Jr., Feig, M., and Brooks, C.L., 3rd. (2004). Extending the treatment of backbone energetics in protein force fields: limitations of gas-phase quantum mechanics in reproducing protein conformational distributions in molecular dynamics simulations. J. Comput. Chem. *25*, 1400–1415.

MacKerell, A.D., Bashford, D., Bellot, M., Dunbrack, R.L., Evanseck, J.D., Field, M.J., Fischer, S., Gao, J., Guo, H., Ha, S., et al. (1998). All-atom empirical potential for molecular modeling and dynamics studies of proteins. J. Phys. Chem. B *102*, 3586–3616.

Mindell, J.A., and Grigorieff, N. (2003). Accurate determination of local defocus and specimen tilt in electron microscopy. J. Struct. Biol. *142*, 334–347.

Mizuno, T., Doi, Y., Mizoguchi, H., Jin, S., Noda, M., Sonobe, Y., Takeuchi, H., and Suzumura, A. (2011). Interleukin-34 selectively enhances the neuroprotective effects of microglia to attenuate oligomeric amyloid-β neurotoxicity. Am. J. Pathol. *179*, 2016–2027.

Nishikawa, I., Nakajima, Y., Ito, M., Fukuchi, S., Homma, K., and Nishikawa, K. (2010). Computational prediction of O-linked glycosylation sites that preferentially map on intrinsically disordered regions of extracellular proteins. Int. J. Mol. Sci. *11*, 4991–5008.

Pernot, P., Theveneau, P., Giraud, T., Fernandes, R.N., Nurizzo, D., Spruce, D., Surr, J., McSweeney, S., Round, A., Felisaz, F., et al. (2010). New beamline dedicated to solution scattering from biological macromolecules at the ESRF. J. Phys. Conf. Ser. *247*, 012009.

Petoukhov, M.V., and Svergun, D.I. (2005). Global rigid body modeling of macromolecular complexes against small-angle scattering data. Biophys. J. *89*, 1237–1250.

Petoukhov, M.V., Franke, D., Shkumatov, A.V., Tria, G., Kikhney, A.G., Gajda, M., Gorba, C., Mertens, H.D.T., Konarev, P.V., and Svergun, D.I. (2012). New developments in the ATSAS program package for small-angle scattering data analysis. J. Appl. Cryst. *45*, 342–350.

Phillips, J.C., Braun, R., Wang, W., Gumbart, J., Tajkhorshid, E., Villa, E., Chipot, C., Skeel, R.D., Kalé, L., and Schulten, K. (2005). Scalable molecular dynamics with NAMD. J. Comput. Chem. *26*, 1781–1802.

Rathore, Y.S., Rehan, M., Pandey, K., Sahni, G., and Ashish. (2012). First structural model of full-length human tissue-plasminogen activator: a SAXS data-based modeling study. J. Phys. Chem. B *116*, 496–502.

Reeves, P.J., Callewaert, N., Contreras, R., and Khorana, H.G. (2002). Structure and function in rhodopsin: high-level expression of rhodopsin with restricted and homogeneous N-glycosylation by a tetracycline-inducible N-acetylglucosaminyltransferase I-negative HEK293S stable mammalian cell line. Proc. Natl. Acad. Sci. USA *99*, 13419–13424.

Roessle, M.W., Klaering, R., Ristau, U., Robrahn, B., Jahn, D., Gehrmann, T., Konarev, P., Round, A., Fiedler, S., Hermes, C., et al. (2007). Upgrade of the small-angle X-ray scattering beamline X33 at the European Molecular Biology Laboratory, Hamburg. J. Appl. Cryst. *40*, s190–s194.

Roy, A., Kucukural, A., and Zhang, Y. (2010). I-TASSER: a unified platform for automated protein structure and function prediction. Nat. Protoc. *5*, 725–738.

Ruch, C., Skiniotis, G., Steinmetz, M.O., Walz, T., and Ballmer-Hofer, K. (2007). Structure of a VEGF-VEGF receptor complex determined by electron microscopy. Nat. Struct. Mol. Biol. *14*, 249–250.

Schneidman-Duhovny, D., Hammel, M., and Sali, A. (2010). FoXS: a web server for rapid computation and fitting of SAXS profiles. Nucleic Acids Res. *38*(Web Server issue), W540–W544.

Svergun, D. (1992). Determination of the regularization parameter in indirect-transform methods using perceptual criteria. J. Appl. Cryst. *25*, 495–503.

Svergun, D.I. (1999). Restoring low resolution structure of biological macromolecules from solution scattering using simulated annealing. Biophys. J. *76*, 2879–2886.

Svergun, D., Barberato, C., and Koch, M.H.J. (1995). CRYSOL-a program to evaluate X-ray solution scattering of biological macromolecules from atomic coordinates. J. Appl. Cryst. *28*, 768–773.

Tanner, D.E., Chan, K.-Y., Phillips, J.C., and Schulten, K. (2011). Parallel generalized born implicit solvent calculations with NAMD. J. Chem. Theory Comput. *7*, 3635–3642.

Van den Steen, P., Rudd, P.M., Dwek, R.A., and Opdenakker, G. (1998). Concepts and principles of O-linked glycosylation. Crit. Rev. Biochem. Mol. Biol. *33*, 151–208.

van Heel, M., Harauz, G., Orlova, E.V., Schmidt, R., and Schatz, M. (1996). A new generation of the IMAGIC image processing system. J. Struct. Biol. *116*, 17–24.

Verstraete, K., and Savvides, S.N. (2012). Extracellular assembly and activation principles of oncogenic class III receptor tyrosine kinases. Nat. Rev. Cancer *12*, 753–766.

Verstraete, K., Remmerie, B., Elegheert, J., Lintermans, B., Haegeman, G., Vanhoenacker, P., Van Craenenbroeck, K., and Savvides, S.N. (2011a). Inducible production of recombinant human Flt3 ectodomain variants in mammalian cells and preliminary crystallographic analysis of Flt3 ligand-receptor complexes. Acta Crystallogr. Sect. F Struct. Biol. Cryst. Commun. *67*, 325–331.

Verstraete, K., Vandriessche, G., Januar, M., Elegheert, J., Shkumatov, A.V., Desfosses, A., Van Craenenbroeck, K., Svergun, D.I., Gutsche, I., Vergauwen, B., and Savvides, S.N. (2011b). Structural insights into the extracellular assembly of the hematopoietic Flt3 signaling complex. Blood *118*, 60–68.

Volkov, V.V., and Svergun, D.I. (2003). Uniqueness of ab initio shape determination in small-angle scattering. J. Appl. Cryst. *36*, 860–864.

Wang, Y., Szretter, K.J., Vermi, W., Gilfillan, S., Rossini, C., Cella, M., Barrow, A.D., Diamond, M.S., and Colonna, M. (2012). IL-34 is a tissue-restricted ligand of CSF1R required for the development of Langerhans cells and microglia. Nat. Immunol. *13*, 753–760.

Wei, S., Nandi, S., Chitu, V., Yeung, Y.-G., Yu, W., Huang, M., Williams, L.T., Lin, H., and Stanley, E.R. (2010). Functional overlap but differential expression of CSF-1 and IL-34 in their CSF-1 receptor-mediated regulation of myeloid cells. J. Leukoc. Biol. *88*, 495–505.

Weinkam, P., Pons, J., and Sali, A. (2012). Structure-based model of allostery predicts coupling between distant sites. Proc. Natl. Acad. Sci. USA *109*, 4875–4880.

Yang, Y., Yuzawa, S., and Schlessinger, J. (2008). Contacts between membrane proximal regions of the PDGF receptor ectodomain are required for receptor activation but not for receptor dimerization. Proc. Natl. Acad. Sci. USA *105*, 7681–7686.

Yang, Z.R., Thomson, R., McNeil, P., and Esnouf, R.M. (2005). RONN: the bio-basis function neural network technique applied to the detection of natively disordered regions in proteins. Bioinformatics *21*, 3369–3376.

Yang, Y., Xie, P., Opatowsky, Y., and Schlessinger, J. (2010). Direct contacts between extracellular smembrane-proximal domains are required for VEGF receptor activation and cell signaling. Proc. Natl. Acad. Sci. USA *107*, 1906–1911.

Yuzawa, S., Opatowsky, Y., Zhang, Z., Mandiyan, V., Lax, I., and Schlessinger, J. (2007). Structural basis for activation of the receptor tyrosine kinase KIT by stem cell factor. Cell *130*, 323–334.

Zeev-Ben-Mordehai, T., Mylonas, E., Paz, A., Peleg, Y., Toker, L., Silman, I., Svergun, D.I., and Sussman, J.L. (2009). The quaternary structure of amalgam, a Drosophila neuronal adhesion protein, explains its dual adhesion properties. Biophys. J. *97*, 2316–2326.